# Terahertz-mediated microwave-to-optical transduction

Furkan Sahbaz,[1,3] James N. Eckstein,[2,3] Dale J. Van Harlingen,[2,3] and Simeon I. Bogdanov[1,3]
[1]*Department of Electrical and Computer Engineering, and Nick Holonyak, Jr. Micro and Nanotechnology Laboratory, University of Illinois at Urbana-Champaign, Urbana, Illinois 60801, USA*
[2]*Department of Physics and Materials Research Laboratory, University of Illinois at Urbana Champaign, Urbana, Illinois 81801, USA*
[3]*Illinois Quantum Information Science and Technology Center, University of Illinois Urbana-Champaign, Urbana, Illinois 61801, USA*

(Received 7 July 2023; revised 25 October 2023; accepted 6 March 2024; published 10 April 2024)

Transduction of quantum signals between the microwave and the optical ranges will unlock powerful hybrid quantum systems enabling information processing with superconducting qubits and low-noise quantum networking through optical photons. Most microwave-to-optical quantum transducers suffer from thermal noise due to pump absorption. We analyze the coupled thermal and wave dynamics in electro-optic transducers that use a two-step scheme based on an intermediate frequency state in the THz range. Our analysis, supported by numerical simulations, shows that the two-step scheme operating with a continuous pump offers near-unity external efficiency with a multiorder noise suppression compared to single-step transduction. As a result, two-step electro-optic transducers may enable quantum-noise-limited interfacing of superconducting quantum processors with optical channels at MHz-scale bit rates.

DOI: 10.1103/PhysRevA.109.042409

## I. INTRODUCTION

Superconducting qubits are prime candidates for scalable quantum information processing, while optical photons offer long-distance transmission of quantum states in ambient conditions. Faithful conversion of quantum states between microwave and optical frequency ranges, called quantum transduction, is instrumental in bridging the gap between these complementary functionalities. For example, optical interconnects transmitting information between individual superconducting quantum processors will enable distributed quantum computing. Conversely, superconducting quantum processors integrated into quantum optical networks will equip the latter with deterministic quantum gates and error correction [1].

The key figures of merit for a microwave-to-optical quantum transducer are the conversion efficiency $\eta$, added noise $n_\mu$, and bandwidth $\Delta\omega$ [2–4]. Limits on $\eta$ and $n_\mu$ are dictated by the error-correction thresholds, while $\Delta\omega$ must accommodate the qubit decoherence rates that are typically in the kHz range [1,5]. In recent experiments, microwave-to-optical quantum transduction has been realized with optomechanical [6–9], spin wave [10–12], atom-assisted [13–15], and electro-optic (EO) [16–25] interfaces. However, no platform to date has reached quantum-limited microwave-to-optical transduction, i.e., combine a near-unity efficiency with added noise below the single-photon level ($n_\mu \ll 1$), at MHz bandwidths.

EO microwave-to-optical transducers stand out thanks to their integration-friendly architectures and bandwidths of tens of MHz, comparable with the inverse gate times. They are realized by combining nonlinear optical materials with three-dimensional (3D) [18–21] or planar [22–25] superconducting microwave resonators. A strong optical pump $p_o$ propagating in the nonlinear material mediates the interaction between a microwave mode $s_\mu$ and an optical sideband mode $s_o$, as shown in Figs. 1(a) and 1(b). Due to weak nonlinearities in the optical range and the large wavelength mismatch, pump powers exceeding 1 W are typically required for efficient EO conversion. Even the absorption of a minute fraction of pump photons leads to a prohibitively strong thermal microwave photon generation and excess losses in optical and microwave modes, affecting both $\eta$ and $n_\mu$. Recent works on mm-wave superconducting circuits suggest that they can be a viable stepping stone for microwave-to-optical transduction [15,26,27]. Most recently, mm-wave-to-optical transduction using neutral atoms has shown attractive noise and efficiency figures of merit [15]. Here we show that transducing photons from the microwave to the optical range through an intermediate high-frequency state can help overcome the fundamental limitations of single-step EO transducers. Specifically, we analyze a scenario where the microwave photon is first upconverted to an intermediate frequency by using kinetic inductance nonlinearity in niobium nitride (NbN), and then it is upconverted to the optical range through the second-order optical nonlinearity in lithium niobate (LN). By studying the noise scaling as a function of the intermediate frequency $\omega_i$ and waveguide dimensions, we show that this two-step transduction reduces the thermal noise by orders of magnitude while maintaining near-unity conversion efficiency. We confirm the model validity by numerically simulating the transduction from 8 GHz to 200 THz through an intermediate frequency state in a NbN-based two-step transducer. The proposed approach promises transduction with quantum-limited performance at MHz-scale conversion rates.

## II. HEAT SCALING IN ELECTRO-OPTIC TRANSDUCERS

First, we analyze the noise and efficiency scaling laws of single-step EO transduction mediated by electro-optic

 

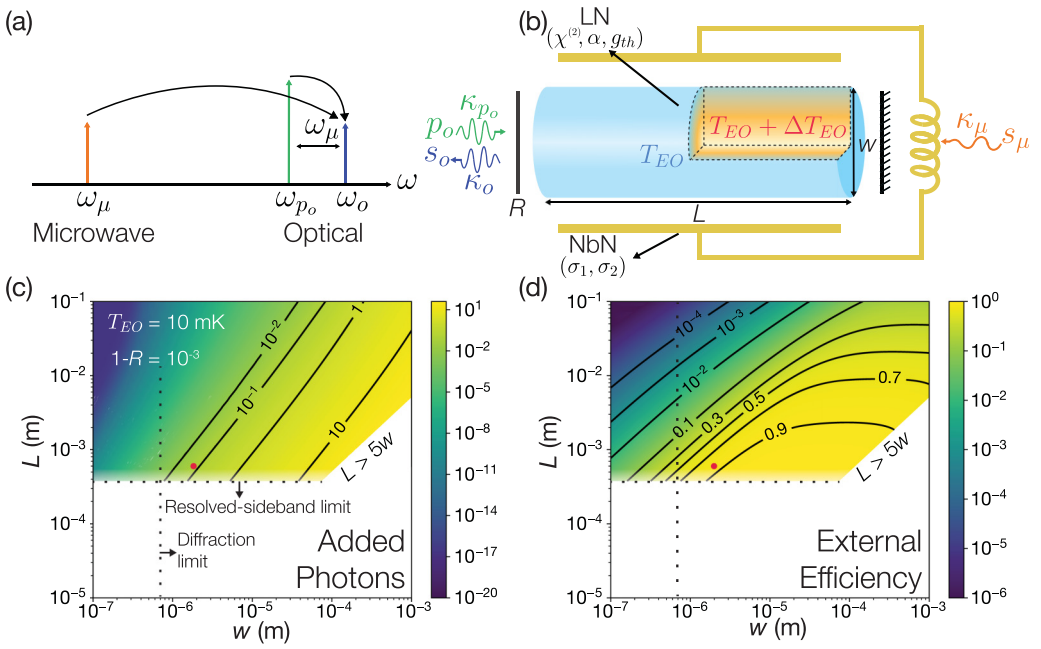


FIG. 1. (a) Single-step EO quantum transduction in the frequency domain. (b) Schematic of an EO transducer model consisting of a LN optical resonator with coupling parameter $1-R$, cross-section diameter $w$, and length $L$, integrated with a superconducting NbN resonator. The heating $\Delta T_{\rm EO}$ is caused by optical pump absorption in LN. The thermal transport is assumed to be radial. (c) The microwave mode occupancy and (d) the external conversion efficiency as a function of $w$ and $L$ for $\omega_\mu = 2\pi \times 8$ GHz, $1 - R = 10^{-3}$, and base temperature $T_{\rm EO} = 10$ mK, at unity cooperativity. The red dot marks the numerically simulated geometry for microwave-to-optical transduction.

nonlinearity ($\chi^{(2)}$). Specifically, we calculate the thermal microwave mode occupancy, $n_{\mu,1}$, and the external transduction efficiency, $\eta_1$, in integrated resonators according to a simple analytical model (see Table I for a summary of notations). We consider a microwave NbN resonator, interacting with an optical LN resonator in a nonlinear region of round-trip length $L$ and width $w$. The pump signal $p_o$ (at $\omega_{p_o} = 2\pi \times 200$ THz) mixes with $s_\mu$ (at $\omega_\mu = 2\pi \times 8$ GHz) to obtain the sideband $s_o$ as in Figs. 1(a) and 1(b). We initially assume unity electro-optic cooperativity [$C_{\rm EO} = 4g_{\rm EO}^2|p_o|^2/(\kappa_\mu\kappa_o) = 1$], where $g_{\rm EO}$, $|p_o|^2$, $\kappa_\mu$, are $\kappa_o$ are the EO coupling rate, number of pump photons, and loss rates for microwave and optical modes, respectively (see Appendix A). The losses in all of the modes consist of internal (absorption) and external (outcoupling) loss rates: $\kappa_\mu = \kappa_{\mu,i} + \kappa_{\mu,e}$, $\kappa_o = \kappa_{o,i} + \kappa_{o,e}$, and $\kappa_o = \kappa_{p,i} + \kappa_{p,e}$ [17]. To gain additional insight, we assume unity spatial overlap between the modes $p_o$, $s_\mu$, and $s_o$ in analytical calculations, but take the finite overlap into account in the numerical simulations presented below. Explicit values and expressions of all the geometric and material parameters involved are given in Appendixes A and B. The coupling coefficient, $1 - R = 10^{-3}$ of the optical resonator is chosen so that the transducer is overcoupled but remains in the resolved-sideband regime, i.e., $\kappa_{p_o}/\omega_\mu < 0.01$. Additional results for $1 - R = 10^{-2}$ and $10^{-4}$ are available in Appendix C.

Under the boundary condition $C_{\rm EO} = 1$, the external efficiency simplifies to $\eta_1 = \kappa_{\mu,e}\kappa_{o,e}/(\kappa_\mu\kappa_o)$. The thermal

TABLE I. Summary of parameters used in the transducer analysis.

| Symbol | Quantity | Symbol | Quantity |
|---|---|---|---|
| $s_\mu$ | Microwave signal | $\omega_\mu$ | Microwave frequency |
| $p_o$ | Pump signal (optical) | $\omega_{p_o}$ | Pump frequency (optical) |
| $s_o$ | Sideband signal (optical) | $\omega_o$ | Optical sideband frequency |
| $s_i$ | Intermediate signal | $\omega_{p_i}$ | Pump frequency (intermediate) |
| $p_i$ | Pump signal (intermediate) | $\omega_i$ | Intermediate frequency |
| $\kappa_\mu$ | Microwave loss rate | $n_{\mu,1}$ | Single-step occupancy |
| $\kappa_{p_o}$ | Pump loss rate (optical) | $\eta_1$ | Single-step efficiency |
| $\kappa_o$ | Sideband loss rate (optical) | $n_{\mu,2}$ | Two-step occupancy |
| $\kappa_i$ | Intermediate loss rate | $\eta_2$ | Two-step efficiency |
| $\kappa_{p_i}$ | Pump loss rate (intermediate) | $T_{\rm KI}$ | Kinetic inductance step base temperature |
| $g_{\rm EO}$ | Electro-optic step coupling rate | $T_{\rm EO}$ | Electro-optic step base temperature |
| $g_{\rm KI}$ | Kinetic inductance step coupling rate | $\Delta T_{\rm KI,EO}$ | Pump-induced heating |

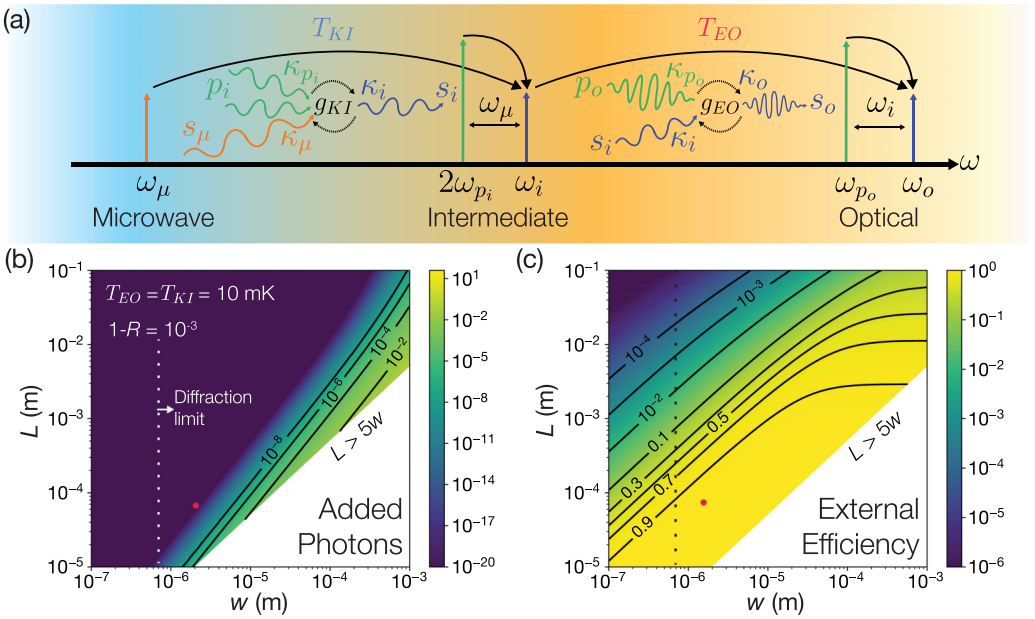


FIG. 2. (a) Two-step transduction using the kinetic inductance and electro-optic nonlinearities. (b) The intermediate frequency mode occupancy and (c) the external conversion efficiency as a function of $w$ and $L$ for $\omega_i = 2\pi \times 600$ GHz, $1 - R = 10^{-3}$, and base temperatures $T_{\mathrm{KI}} = T_{\mathrm{EO}} = 10$ mK at unity cooperativity. The red dot marks the numerically simulated geometry for two-step transduction via 600 GHz.

microwave mode occupancy is calculated by assuming the microwave mode is coupled to the cryostat environment with base temperature $T_{\mathrm{EO}}$ and the bath of the active medium (LN) at a temperature $T_{\mathrm{EO}} + \Delta T_{\mathrm{EO}}$ heated by pump absorption. The thermal Bose-Einstein occupation factors due to the cryostat environment $[n_E(\mathrm{T_{EO}})]$ and the bath $[n_B(T_{\mathrm{EO}} + \Delta T_{\mathrm{EO}})]$ add up to the total thermal microwave mode occupancy $n_{\mu 1} = n_B(T_{\mathrm{EO}} + \Delta T_{\mathrm{EO}})\kappa_{\mu,e}/\kappa_\mu + n_E(T_{\mathrm{EO}})\kappa_{\mu,i}(T_{\mathrm{EO}} + \Delta T_{\mathrm{EO}})/\kappa_\mu$ [28,29].

$n_{\mu 1}$ and $\eta_1$ are thus determined by active medium temperature $T_{\mathrm{EO}} + \Delta T_{\mathrm{EO}}$ through the strongly temperature-dependent microwave losses and the Bose-Einstein occupation factor. The heating $\Delta T_{\mathrm{EO}}$ is induced by the pump photons with total energy $|p_o|^2\hbar\omega_{p_o}$ uniformly distributed over the transducer volume and absorbed at a rate $\kappa_{p,i}$. We assume radial heat transfer from the transducer's nonlinear region to the cladding material, which is a good approximation when $L \gg w$. In this model, we describe the heat transport with a common thermal conductivity value $g_{\mathrm{th}}(T_{\mathrm{EO}} + \Delta T_{\mathrm{EO}})$ equal to that of LN. We calculate the heating in the regime of continuous wave (cw) pumping guaranteeing maximum conversion bandwidth, which leads to $\Delta T_{\mathrm{EO}} = |p_o|^2\hbar\omega_{p_o}\kappa_{p,i}/g_{\mathrm{th}}L$. Under the $C_{\mathrm{EO}} = 1$ constraint, $\Delta T_{\mathrm{EO}}$ obeys the following steady-state equation [30,31]:

$$\Delta T_{\mathrm{EO}} = \frac{\kappa_\mu(T_{\mathrm{EO}} + \Delta T_{\mathrm{EO}})\kappa_o}{4g_{\mathrm{EO}}^2}\frac{\hbar\omega_{p_o}\kappa_{p_o,i}}{g_{\mathrm{th}}(T_{\mathrm{EO}} + \Delta T_{\mathrm{EO}})L}. \quad (1)$$

This implicit equation highlights the difficulty of achieving quantum-limited performance. Heating leads to excess microwave loss $\kappa_\mu$, which, through the $C_{\mathrm{EO}} = 1$ constraint, requires a higher pump power, leading to even more heating. Low operating temperatures present an additional challenge as the thermal conductivities of most materials vanish (see Appendix B). Figures 1(c) and 1(d) plot $\eta_1$ and $n_{\mu,1}$ as a function of transducer dimensions $w$ and $L$, at $T_{\mathrm{EO}} = 10$ mK. Figure 1(c) indicates that the region of highest efficiency for the single-step transducer strongly overlaps with the region of high thermal noise population. In agreement with previous works [18–25], the heating caused by the optical pump is reduced in longer resonators, but so is the external efficiency. Narrowing $w$ improves the coupling rate $g_{\mathrm{EO}}$, reducing the optical pumping requirements, and exponentially suppressing the noise photon population. However, in practice, $w$ cannot be reduced much below the pump wavelength $w \sim 2\pi c/n_{\mathrm{LN}}\omega_{p_o}$ without causing a significant pump spillage into the superconductor, where $n_{\mathrm{LN}}$ is the LN refractive index at $\omega_{p_o}$.

## III. TWO-STEP QUANTUM TRANSDUCTION

The above analysis suggests that, by substituting the temperature in the Bose-Einstein occupation factor $n = (e^{\hbar\omega_\mu/[k_{\mathrm{B}}(T_{\mathrm{EO}}+\Delta T_{\mathrm{EO}})]} - 1)^{-1}$ using Eq. (1), the noise photon population scales exponentially with the ratio $\omega_\mu/\omega_{p_o}$. Thus the noise can be significantly reduced by introducing an intermediate mode $s_i$ with a frequency $\omega_i$ such that $\omega_\mu \ll \omega_i \ll \omega_o$, and performing the transduction in two steps [$s_\mu$ to $s_i$, then $s_i$ to $s_o$, Fig. 2(a)]. The fundamental advantage of this scheme comes from its intrinsic resources for minimizing thermal noise. Specifically, the first step ($s_\mu \to s_i$) is pumped by photons of relatively low energy $\hbar\omega_{p_i} \ll \hbar\omega_{p_o}$, which minimizes the associated heating. The second step ($s_i \to s_o$) starts from a frequency $\omega_i \gg \omega_\mu$, making it less sensitive to the heating. In addition, the coupling rates of both steps increase with $\omega_i$, reducing the pump intensity requirement compared to the single-step transduction.

Superconductor-insulator-superconductor (SIS) mixers [32–36] and kinetic inductance (KI) nonlinearity have been proposed to enable quantum-limited frequency conversion between the microwave and 0.1–1 THz ranges

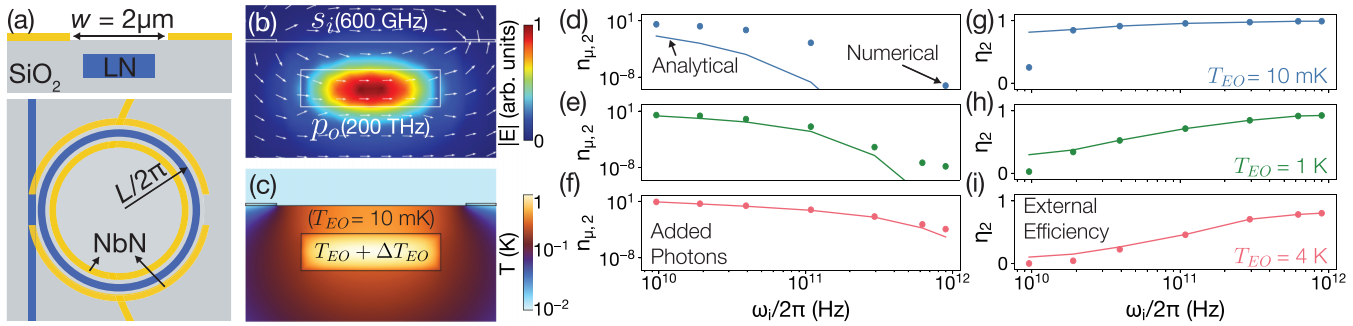


FIG. 3. (a) Cross section and top view of simulated second-step transducer, consisting of a superconducting NbN resonator whose capacitor rings are placed around a LN ring resonator. The NbN resonator also contains a larger inductive ring whose radius is determined by the operating wavelength. Cross-sectional profiles for (b) $s_i$ and $p_o$ fields and (c) $\Delta T_{\mathrm{EO}}$. Colors in (b) represent the electric field norm corresponding to an optical pump in linear scale, and the arrows represent intermediate-frequency electric field strength and direction. Colors in (c) represent the temperature distribution in logarithmic scale. Analytical and numerical calculations of (d)–(f) mode occupancy and (g)–(i) external conversion efficiency of the EO step at 10 mK, 1 K, and 4 K.

[26,27,37–40]. Here we consider a KI-based mixer to implement the first step ($s_\mu \rightarrow s_i$) and an EO mixer as described earlier to implement the second step ($s_i \rightarrow s_o$), as shown in Fig. 2(a). Similarly, the intermediate pump $p_i$ [at $\omega_{p_i} = (\omega_i - \omega_\mu)/2 = 2\pi \times 296\,\mathrm{GHz}$] and $s_\mu$ interact to generate the intermediate-frequency signal $s_i$. The cooperativity of the KI-mediated interaction is defined as $C_{\mathrm{KI}} = 4g_{\mathrm{KI}}^2|p_i|^4/\kappa_\mu\kappa_i$, where $\kappa_\mu$ and $\kappa_i$ are the loss rates of the microwave mode and the intermediate mode, respectively, and $g_{\mathrm{KI}}$ is the KI coupling rate (Appendix A). We analyze the cascaded performance of the two steps under the boundary condition $C_{\mathrm{KI}} = C_{\mathrm{EO}} = 1$, where we redefine $C_{\mathrm{EO}} = 4g_{\mathrm{EO}}^2|p_o|^2/\kappa_i\kappa_o$.

To directly compare the performance of the two-step transducer to that of a single-step one, we first consider the base temperatures of the two steps to be equal: $T_{\mathrm{KI}} = T_{\mathrm{EO}} = 10$ mK. The estimated temperature increase in the KI step ($\Delta T_{\mathrm{KI}}$) minimally affects the noise and efficiency of the two-step scheme, as demonstrated in Appendix D. Therefore, by locking in the parameters of the first step [Fig. 8(a)], we focus our comparison on the performance of the second step.

In Figs. 2(b) and 2(c) we plot the efficiency $\eta_2$ and thermal mode occupancy $n_{\mu,2}$ of the two-step transducer with $\omega_i = 600$ GHz, assuming unity cooperativity, as a function of the length $L$ and the width $w$ of the second-step converter. The second-step coupling parameter $1–R$ is again fixed to $10^{-3}$ to satisfy $\kappa_{p_o}/\omega_i < 0.01$. In the region of the red dot in Figs. 2(b) and 2(c), we observe a multiorder reduction in noise photon occupancy $n_{\mu,2}$ and a higher efficiency compared to those of a single-step transducer [Figs. 1(c) and 1(d)], mainly conditioned by a strong increase in $g_{\mathrm{EO}}$. The wide region of quantum-limited performance allows a vast design freedom in terms of $L$, $w$, and $1-R$ (see Appendix C).

To validate the analytical results, we performed finite element simulations of interacting resonator modes and heat transfer in the performance-limiting EO step as a function of the intermediate frequency $\omega_i$ using COMSOL MULTIPHYSICS with material properties listed in Appendix B. In our numerical models, we integrate a LN ring resonator with parallel electrodes of a NbN superconducting resonator in a triply resonant setup [22–25,41,42], as illustrated in Figs. 3(a)–3(c). To select parameter values, we note that the device performance favors smaller interaction region dimensions $w$ and $L$ (Figs. 1 and 2). In practice, lower limits on $w$ and $L$ are dictated by optical diffraction and bending loss-limited optical quality factor, respectively [43–46]. Considering these limits, we choose parameters listed in Table II for our numerical simulations, as they maximize the device performance in the resolved-sideband limit. The simulated optical resonators are placed 0.5 μm below the superconducting electrodes, and the electrode gap is set to 2 μm to minimize pump mode overlap with the superconductor.

Numerical results in Figs. 3(d) and 3(g) (dots) confirm the analytical trends described by Eq. (1) (solid lines). At low $\omega_i$, the discrepancy between the numerical and analytical data in Figs. 3(d) and 3(g) (between solid lines and dots) can be explained by imperfect mode overlap between modes $s_i$ and $p_o$. The analytically estimated pump photon number $|p_o|^2$ on the order of $10^4$ increases to $10^8$ in numerical calculations that account for the mode overlap. This has a strong impact on device performance: for example, at $\omega_i = 2\pi \times 10$ GHz the efficiency drops over 3 times, while the added photon noise increases by almost two orders. At higher intermediate frequencies $\omega_i > 2\pi \times 100$ GHz, the performance is intrinsically less sensitive to heating, and, additionally, the mode overlap in numerically simulated devices improves. As a result, both analytical and numerical models match in predicting an improved device performance by several orders of magnitude with optical pump powers in the mW range.

Moreover, the loss rates listed in Table II indicate that the bandwidth of the second step, given by $\min(\kappa_i, \kappa_o)$, increases by up to two orders of magnitude at higher $\omega_i$. The transduction response is therefore limited by the KI-based transducer bandwidth, which is in the range of 10 MHz [26,27]. As a result, the two-step scheme is capable of transducing at rates much faster than qubit decoherence rates [5].

Since $\omega_i$ can be chosen to be much higher than $\omega_\mu$, one can operate the EO transduction step at higher base temperatures than the KI step. Thus the EO step can be placed away from the mK cryostat chamber, isolating the latter from all optical signals, and suppressing numerous deleterious optical absorption-related effects [47,48]. Numerical and analytical simulations at $T_{\mathrm{EO}} = 1$ K and $T_{\mathrm{EO}} = 4$ K [Figs. 3(e) and 3(h) and Figs. 3(f) and 3(i), respectively) confirm this hypothesis:

TABLE II. Key parameters of numerically simulated resonators in the second transduction step.

| $\omega_i$ Intermediate frequency | $L$ Resonator length | $w$ Resonator width | $g_{\mathrm{EO}}$ EO coupling rate | $\kappa_o$ Optical loss rate | $\kappa_i$ Loss rate at $\omega_i$ |
|---|---|---|---|---|---|
| 9.5 GHz | $2\pi \times 100\,\mu$m | | 1.93 kHz | 80.97 MHz | 1.77 MHz |
| 19 GHz | $2\pi \times 100\,\mu$m | | 5.17 kHz | 80.97 MHz | 4.86 MHz |
| 39.2 GHz | $2\pi \times 50\,\mu$m | | 13.2 kHz | 80.97 MHz | 18.62 MHz |
| 108.3 GHz | $2\pi \times 15\,\mu$m | 2 μm | 50.65 kHz | 139.86 MHz | 0.11 GHz |
| 294 GHz | $2\pi \times 15\,\mu$m | | 198.66 kHz | 139.86 MHz | 0.97 GHz |
| 622.4 GHz | $2\pi \times 10\,\mu$m | | 487.85 kHz | 0.88 GHz | 2.42 GHz |
| 863.2 GHz | $2\pi \times 10\,\mu$m | | 665.88 kHz | 0.88 GHz | 3.81 GHz |

at $\omega_i > 300$ GHz, the two-step transducer can still maintain nearly quantum-limited efficiency and noise performance.

The impact of pump-induced heating on device performance can be partially alleviated by reducing the cooperativity. Figure 4 plots mode occupancy and external efficiency for cooperativity values between $10^{-2}$ and 0.5. In Appendix E, we also estimate the fidelity [49–51] and quantum channel capacity [52–56] based on these figures. Two-step transduction features a multiorder noise suppression at all cooperativities, but its practical advantage is the most significant for cooperativities above 0.1 where the channel capacity is nonzero.

## IV. DISCUSSION

THz-mediated transducers promise a coherent transfer of quantum states between stationary qubits and generating entanglement with rates higher than the qubit decoherence rates, which enables modular quantum computing and network architectures [1]. The attainable performance is characterized by a near-unity fidelity and quantum channel capacity on the order of 10.

Two-step transducers can be further improved through optimized choices of materials, design, and operating regime. Using superconducting materials with critical temperatures higher than that of NbN may help further reduce losses at the intermediate frequency, and allow higher base temperatures, associated with more efficient cooling [57]. In addition, the nonlinear interaction rates can be enhanced by dc-biasing the KI step (three-wave mixing) [39] and using materials with stronger EO nonlinearity than LN [58,59]. Alternative transducer designs such as photonic crystal cavities [60] coupled to Fabry-Perot [61] or antenna-based cavities [62] can be explored to improve resonator loss and interaction rates. While we have only analyzed the scaling of thermal noise in the resolved-sideband regime, alternative transduction protocols can be employed to analyze transducer performance beyond this condition to access even higher conversion bandwidth [50].

There has been an increased interest recently in superconducting quantum devices operating in the mm-wave and THz ranges for detection, spectroscopy, and quantum information. Our analysis of the second step suggests that it can be directly used to connect high-frequency superconducting qubits via optical channels [63,64]. Moreover, the recent advances in superconducting mm-wave and THz couplers and waveguides can be leveraged in the future to efficiently interface both transduction steps [40,65]. Beyond quantum transduction protocols, low-noise superconductor-based electro-optic interfaces will find applications in high-bandwidth wireless communications [66], sensing [62], dark matter detection [67], and astrophysics [34,68].

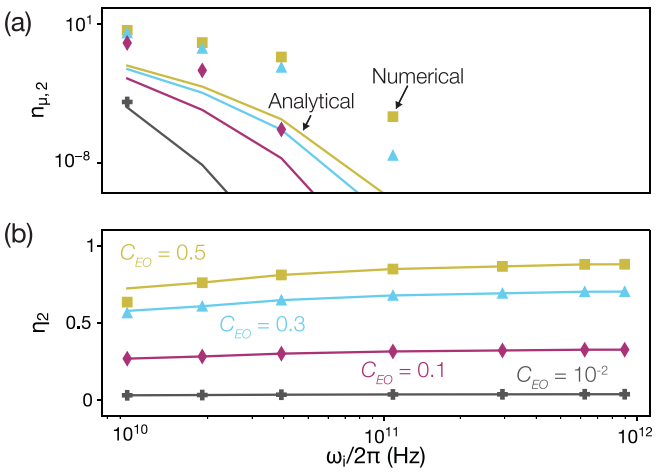


FIG. 4. Analytical and numerical calculations of (a) mode occupancy and (b) external conversion efficiency of the EO step at 10 mK for lower $C_{\mathrm{EO}}$ values of $10^{-2}$, 0.1, 0.3, and 0.5.


## ACKNOWLEDGMENTS

We acknowledge Sary Bseiso for his help in preparing the paper. F.S. and S.I.B. acknowledge the startup funding at the University of Illinois at Urbana-Champaign.


## APPENDIX A: DEFINING NONLINEAR INTERACTIONS AND LOSSES

The interaction between microwave, optical pump, and the optical sideband (as demonstrated in Fig. 1 of the main text) can be described by the beam-splitter interaction Hamiltonian (under rotating wave approximation in the resolved-sideband regime) [16]:

$$H_{\mathrm{int}}^{\mathrm{EO}} = \hbar |p_o| g_{\mathrm{EO}} (s_o^\dagger s_{\mu(i)} + s_o s_{\mu(i)}^\dagger), \tag{A1}$$

where $s_{\mu(i)}$, $p_o$, and $s_o$ are the annihilation operators for the microwave (intermediate), optical pump, and optical sideband modes. The nonlinear coupling rate $g_{\mathrm{EO}}$ can be calculated by

[17]

$$g_{\mathrm{EO}} = \sqrt{\frac{\hbar\omega_{\mu(i)}\omega_{p_o}\omega_o}{8\varepsilon_0\varepsilon_{\mu(i)}\varepsilon_{p_o}\varepsilon_o}}\chi^{(2)}\frac{\int_{\chi^{(2)}} dV E_o^* E_{\mu(i)} E_{p_o}}{\prod_{j=\{\mu(i),p_o,o\}}\sqrt{\int_{\mathrm{all}} dV |E_j|^2}}, \tag{A2}$$

where frequency $\omega_{\mu(i)}$, $\omega_{p_o}$, $\omega_o$; relative permittivity $\varepsilon_{\mu(i)}$, $\varepsilon_{p_o}$, $\varepsilon_o$; and electric field distributions $E_{\mu(i)}$, $E_{p_o}$, $E_o$ are defined for each mode, i.e., microwave (intermediate), optical pump, and optical sideband. The subscript $\mu(i)$ is used to distinguish the lowest-frequency mode depending on the transduction scheme, i.e., single-step (microwave) or two-step (intermediate). Furthermore, efficiency of the electro-optic transduction is given by [16,17]

$$\eta = \frac{4C}{(1+C)^2}\frac{\kappa_{\mu(i),ex}}{\kappa_{\mu(i)}}\frac{\kappa_{o,\mathrm{ex}}}{\kappa_o}. \tag{A3}$$

Here the internal efficiency is defined by the cooperativity parameter $C_{\mathrm{EO}}$ [17]:

$$C_{\mathrm{EO}} = \frac{4g_{\mathrm{EO}}^2|p_o|^2}{\kappa_{\mu(i)}\kappa_o}, \tag{A4}$$

where $\kappa_\mu$, $\kappa_{p_o}$, $\kappa_o$ are the loss rates of each corresponding mode. The loss rate for each mode is determined by the external loss rate and the internal loss rate, i.e., $\kappa_j = \kappa_{j,\mathrm{ex}} + \kappa_{j,\mathrm{in}}$, $j = \{\mu(i), p_o, o\}$.

The kinetic inductance (KI) based upconversion is a four-wave mixing process, where the pump mode is chosen such that $\omega_i = 2\omega_{p_i} + \omega_\mu$. Similar to $H_{\mathrm{int}}^{\mathrm{EO}}$, we can define the interaction Hamiltonian as follows [26]:

$$H_{\mathrm{int}}^{\mathrm{KI}} = \hbar|p_i|^2 g_{\mathrm{KI}}(s_i^\dagger s_\mu + s_i s_\mu^\dagger), \tag{A5}$$

where the new terms $p_i$ and $s_i$ are the annihilation operators for intermediate pump and intermediate state modes. The resulting cooperativity and coupling strength are given by [26,27,69]

$$C_{\mathrm{KI}} = \frac{4g_{\mathrm{KI}}^2|p_i|^4}{\kappa_\mu\kappa_i}, \tag{A6}$$

$$g_{\mathrm{KI}} = \frac{3}{32}\frac{\hbar\omega_{p_i}\sqrt{\omega_\mu\omega_i}}{L_k I_*^2}. \tag{A7}$$

Here $I_*$ and $L_k$ give the scaling current and kinetic inductance, respectively, which are defined by material- and geometry-dependent parameters in Eq. (A8):

$$I_* = \sqrt{\frac{\pi N_0\Delta_0^3}{\hbar\rho}}w't, \tag{A8a}$$

$$L_k = \frac{\hbar\rho}{\pi\Delta_0}\frac{L'}{w't}. \tag{A8b}$$

The length and strip width of the kinetic inductance resonator used in this step are denoted by $L'$ and $w'$, respectively. In addition, $t$, $\Delta_0$, $\mathrm{N}_0$, and $\rho$ are the superconductor thickness, gap energy, electron state density, and normal resistivity of the superconducting materials. To maximize the KI nonlinearity, $t$ is taken as 20 nm in agreement with [27,69].

The internal loss rate of the superconducting resonators is dominated by the superconductor losses:

$$\kappa_{\mu(i),i} = \omega_{\mu(i)}\frac{\sigma_1}{\sigma_2}. \tag{A9}$$

The complex conductivity ($\sigma = \sigma_1 - i\sigma_2$) of superconducting NbN is modeled as a function of frequency and temperature by using material parameters and fitting relations from [70–75] (see Appendix B). The external loss rate is determined by the device geometry [70,76,77].

$$\kappa_{\mu(i),e} = \omega_{\mu(i)}\left(\frac{w}{L}\right)^2, \tag{A10}$$

TABLE III. Material parameters used in analytical and numerical calculations.

| Parameter | Value |
|---|---|
| Absorption coefficient ($\alpha$) of $LiNbO_3$ | 0.84 $cm^{-1}$ at 200 THz [80] |
| | 2 $cm^{-1}$–5 $cm^{-1}$ up to 1.2 THz [81,82] |
| Refractive index of $LiNbO_3$ | 2.3 at 200 THz [80] |
| | 4.9–5 up to 1.2 THz [81] |
| Nonlinear coefficient $r_{33}$ in $LiNbO_3$ | 31 pm $V^{-1}$ [83] |
| Thermal conductivity of $SiO_2$ | 0.0001 W $m^{-1}$ $K^{-1}$ at 10 mK [84] |
| | 0.01 W $m^{-1}$ $K^{-1}$ at 1 K [84] |
| | 0.1 W $m^{-1}$ $K^{-1}$ at 4 K [84] |
| Heat capacity of $SiO_2$ | 0.00001 J $kg^{-1}$ $K^{-1}$ at 10 mK [84] |
| | 0.001 J $kg^{-1}$ $K^{-1}$ at 1 K [84] |
| | 0.01 J $kg^{-1}$ $K^{-1}$ at 4 K [84] |
| Thermal conductivity of NbN | 0.005 W $m^{-1}$ $K^{-1}$ at 10 mK [85] |
| | 5 W $m^{-1}$ $K^{-1}$ T at 1 K [85] |
| | 50 W $m^{-1}$ $K^{-1}$ T at 4 K [85] |
| Heat capacity of NbN | $(0.0283T + 0.0012T^3)$ J $kg^{-1}$ $K^{-1}$ [86] |
| Thermal conductivity of $LiNbO_3$ | $4T^3$ W $m^{-1}$ $K^{-1}$ [87] |
| Heat capacity of $LiNbO_3$ | $2.705 \times 10^{-4}T^3$ J $kg^{-1}$ $K^{-1}$ [87] |
| Critical temperature of NbN ($T_c$) | 16 K [88] |
| Gap energy of NbN at ($\Delta_0$) | $2.075k_BT_c$ [75] |
| Electron state density of NbN ($N_0$) | $1.6 \times 10^{47}$ $J^{-1}$ $m^{-3}$ [75] |

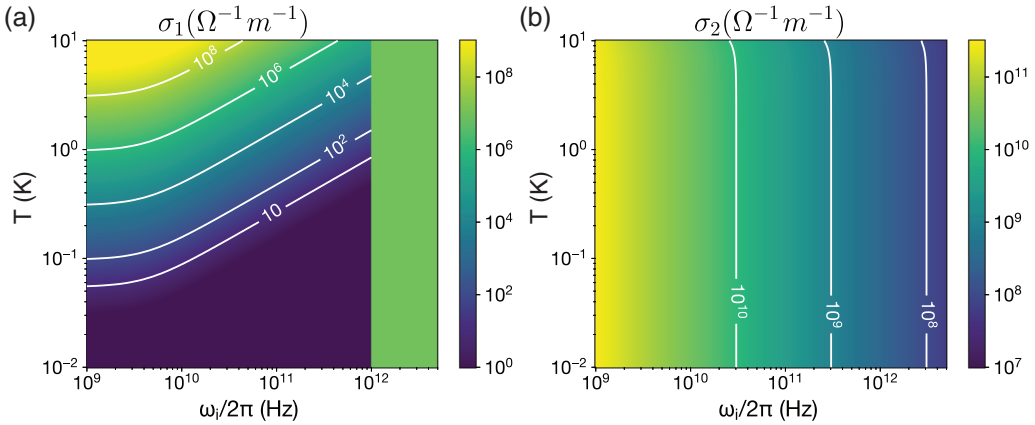


FIG. 5. (a) Real and imaginary parts of complex conductivity from 1 mK to 10 K for NbN [70–75].

where $L$ and $w$ are the length and gap distance of the superconducting device. Furthermore, the loss rate of the optical resonators is calculated through

$$\kappa_{p_o,i} = \frac{\alpha c}{n_g}, \tag{A11a}$$

$$\kappa_{p_o,e} = \frac{(1-R)c}{n_g L}, \tag{A11b}$$

where $c$ is the speed of light, $\alpha$ is the absorption coefficient, $n_g$ is the optical group index, $L$ is the effective optical path length, and $1–R$ is the optical coupling coefficient [46,78,79].

## APPENDIX B: MATERIAL PARAMETERS

Listed below in Table III and Fig. 5 are the specific values used in the analytical and numerical analyses presented in the main text. $\sigma_1(T,\omega)$ and $\sigma_2(T,\omega)$ maps and the $g_{\text{th}}(T)$ dependence were used to solve Eq. (1) in a self-consistent manner. In addition, heat capacity values of LN, $SiO_2$, and NbN are used in the numerical calculations of heat transfer.

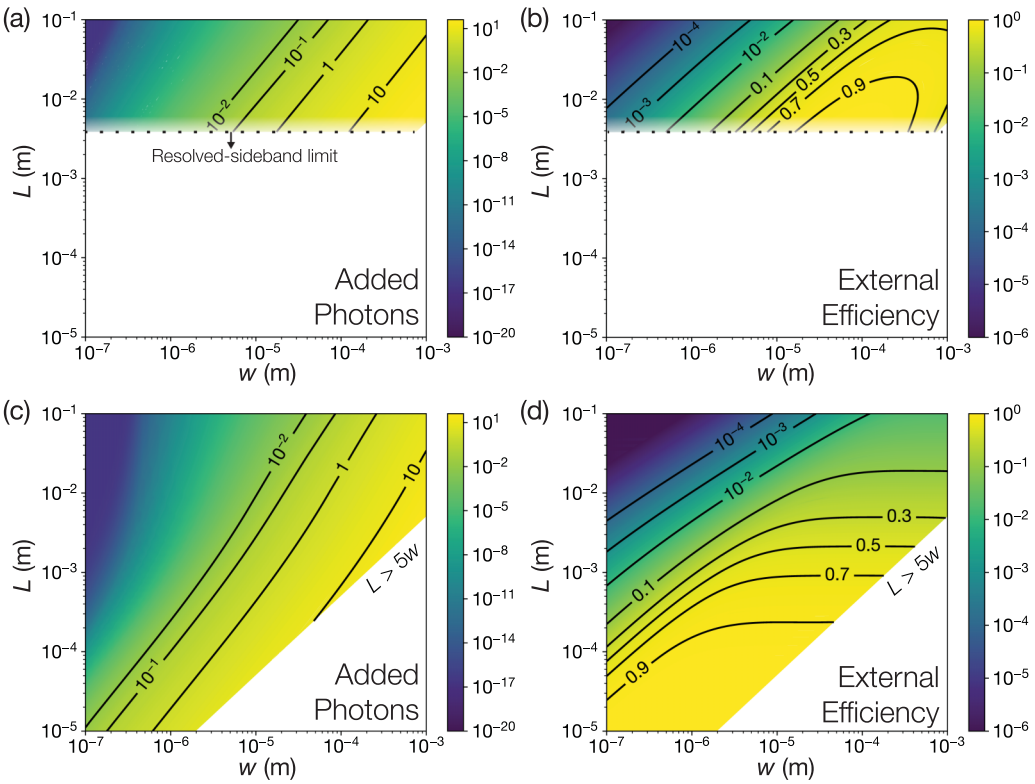


FIG. 6. Extended single-step transduction calculations of mode occupancy and external conversion efficiency for $1 – R = 10^{-2}$ (a,b) and $1 – R = 10^{-4}$ (c,d). The shaded regions in (a,b) are no longer strictly in the resolved-sideband regime.

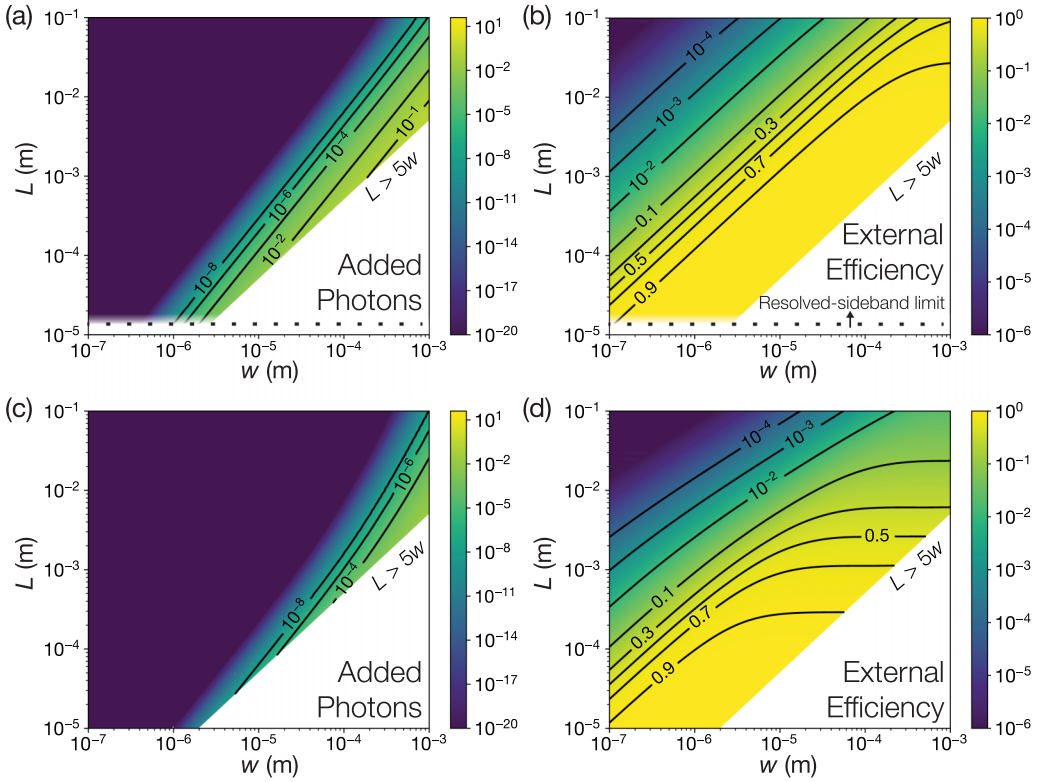


FIG. 7. Extended two-step transduction calculations of mode occupancy and external conversion efficiency for $1 - R = 10^{-2}$ (a), (b) and $1 - R = 10^{-4}$ (c), (d). The shaded regions in (a), (b) are no longer strictly in the resolved-sideband regime.

## APPENDIX C: TRANSDUCTION PERFORMANCE FOR $1 - R = 10^{-2}$ AND $10^{-4}$

Here we calculate the figures of merit for single-step transduction (Fig. 6), and two-step transduction via $\omega_i = 2\pi \times 600$ GHz (Fig. 7), for $1 - R$ values of $10^{-2}$ and $10^{-4}$. These calculations show that the improved performance of the two-step transducers extends over a wide device parameter space.

## APPENDIX D: PUMP-INDUCED HEATING

In this section, we analyze the heating $\Delta T_{\mathrm{EO}}$ and $\Delta T_{\mathrm{KI}}$ in the two steps caused by continuous pump absorption assuming $\omega_i = 2\pi \times 600$ GHz (Fig. 8). The heating in the KI step $\Delta T_{\mathrm{KI}}$ is several orders of magnitude below the base temperature $T_{\mathrm{KI}} = 10$ mK. As a result, the first conversion has negligible effect in the two-step transducer performance and can perform with $\eta \sim 0.99$ and $n_\mu \ll 10^{-6}$ with

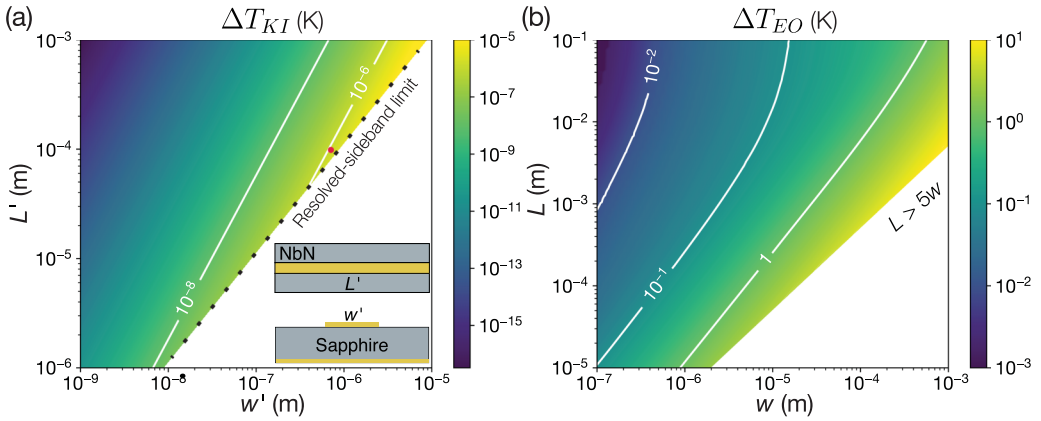


FIG. 8. (a) $\Delta T_{\mathrm{KI}}$ depending on $w\prime$ and $L'$. Inset is the kinetic inductor geometry with 20 nm thickness. The red dot marks a device design that is estimated to perform with $\eta \sim 0.99$ and $n_\mu \ll 10^{-6}$. (b) $\Delta T_{\mathrm{EO}}$ depending on $w$ and $L$.

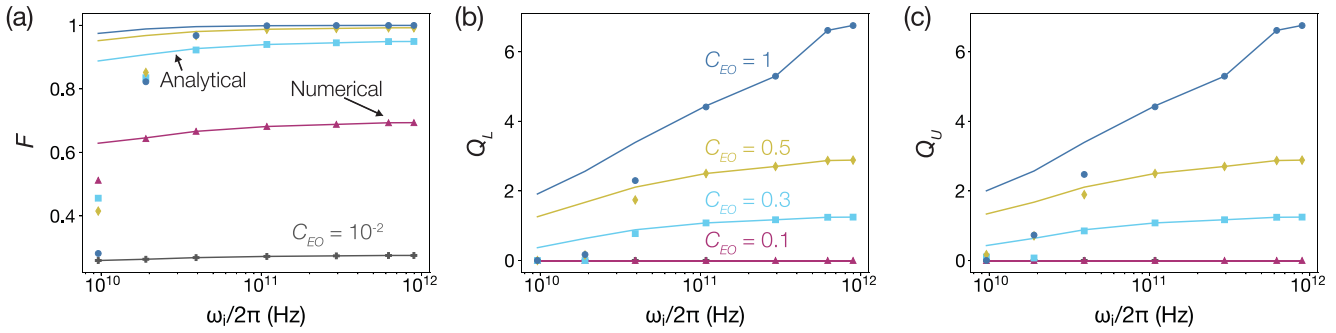


FIG. 9. (a) Transduction fidelity for a coherent state with $|\alpha|^2 = 1$. (b) Lower-bound and (c) upper-bound quantum channel capacity. The straight lines (markers) indicate values estimated based on analytically (numerically) calculated transduction parameters.

parameters marked with the red dot ($L' = 100\,\mu\text{m}$, $w' = 1\,\mu\text{m}$) in Fig. 8(a).

## APPENDIX E: TRANSDUCTION FIDELITY AND QUANTUM CHANNEL CAPACITY

In order to compare the performance of two-step transduction by combining the noise and efficiency figures of merit, we use the design points selected for numerical simulations in Table I of the main text. To estimate the fidelity, we assume an initial coherent state $|\alpha|^2 = 1$ transduced with efficiency $\eta$ and thermal mode occupancy $n_\mu$. The fidelity for this transduction can be expressed through [49–51]

$$F = \frac{1}{1+(1-\eta)n_\mu} e^{-\frac{2[|\alpha|(1-\sqrt{\eta})]^2}{1+(1-\eta)n_\mu}}. \tag{E1}$$

Figure 9(a) shows the fidelities for various cooperativity values, calculated from the analytical (straight lines) and numerical simulation (markers) results. Higher intermediate frequencies result in higher fidelities, reaching over 90% for numerically simulated structures for $\omega_i > 40$ GHz.

We also calculate the upper- and lower-bound estimates on the quantum channel capacity for a thermal-attenuator channel with attenuation coefficient $\eta$ and mean occupancy $n_\mu$. For the lower-bound estimation, we use the derivation provided in [52,56]

$$Q_L = \max\left\{\log_2\left[\frac{\eta}{(1-\eta)}\right] - h(n_\mu), 0\right\}, \tag{E2}$$

where $h(x) = (x+1)\log_2(x+1) - x\log_2 x$. Similarly, we consider derivations from data processing [53], degradable extensions [54] and two-way quantum capacity [55] for the upper-bound estimation [56]:

$$Q_U = \min\{Q_{\text{DP}}, Q_{\text{DE}}, Q_{\text{TW}}\}, \tag{E3a}$$

$$Q_{\text{DP}} = \max\left\{\log_2\left[\frac{\eta-(1-\eta)n_\mu}{(1-\eta)(1+n_\mu)}\right], 0\right\}, \tag{E3b}$$

$$Q_{\text{DE}} = \max\left\{\log_2\left[\frac{\eta}{(1-\eta)}\right] + h[(1-\eta)n_\mu] - h(\eta n_\mu), 0\right\}, \tag{E3c}$$

$$Q_{\text{DE}} = \max\{-\log_2[(1-\eta)\eta^{n_\mu}] - h(n_\mu),\ 0\}. \tag{E3d}$$

The resulting bounds are plotted in Figs. 9(b) and 9(c), respectively, with a trend for improving channel capacity with increasing intermediate frequency. Moreover, at lower cooperativities, the channel capacity vanishes as the overall conversion efficiencies fall below 0.5, indicating that a cooperativity of at least 0.17 should be maintained.


[1] D. Awschalom *et al.*, Development of quantum interconnects (QuICs) for next-generation information technologies, PRX Quantum **2**, 017002 (2021).

[2] N. Lauk, N. Sinclair, S. Barzanjeh, J. P. Covey, M. Saffman, M. Spiropulu, and C. Simon, Perspectives on quantum transduction, Quantum Sci. Technol. **5**, 020501 (2020).

[3] E. Zeuthen, A. Schliesser, A. S. Sørensen, and J. M. Taylor, Figures of merit for quantum transducers, Quantum Sci. Technol. **5**, 034009 (2020).

[4] X. Han, W. Fu, C.-L. Zou, L. Jiang, and H. X. Tang, Microwave-optical quantum frequency conversion, Optica **8**, 1050 (2021).

[5] I. Siddiqi, Engineering high-coherence superconducting qubits, Nat. Rev. Mater. **6**, 875 (2021).

[6] W. Jiang, C. J. Sarabalis, Y. D. Dahmani, R. N. Patel, F. M. Mayor, T. P. McKenna, R. Van Laer, and A. H. Safavi-Naeini, efficient bidirectional piezo-optomechanical transduction between microwave and optical frequency, Nat. Commun. **11**, 1166 (2020).

[7] X. Han *et al.*, Cavity piezo-mechanics for superconducting-nanophotonic quantum interface, Nat. Commun. **11**, 3237 (2020).

[8] M. Mirhosseini, A. Sipahigil, M. Kalaee, and O. Painter, Superconducting qubit to optical photon transduction, Nature (London) **588**, 599 (2020).

[9] B. M. Brubaker, J. M. Kindem, M. D. Urmey, S. Mittal, R. D. Delaney, P. S. Burns, M. R. Vissers, K. W. Lehnert, and C. A. Regal, Optomechanical ground-state cooling in a continuous and efficient electro-optic transducer, Phys. Rev. X **12**, 021062 (2022).

[10] R. Hisatomi, A. Osada, Y. Tabuchi, T. Ishikawa, A. Noguchi, R. Yamazaki, K. Usami, and Y. Nakamura, Bidirectional conver-

sion between microwave and light via ferromagnetic magnons, Phys. Rev. B **93**, 174427 (2016).
[11] J. R. Everts, G. G. G. King, N. J. Lambert, S. Kocsis, S. Rogge, and J. J. Longdell, Ultrastrong coupling between a microwave resonator and antiferromagnetic resonances of rare-earth ion spins, Phys. Rev. B **101**, 214414 (2020).
[12] N. Zhu, X. Zhang, X. Han, C.-L. Zou, C. Zhong, C.-H. Wang, L. Jiang, and H. X. Tang, Waveguide cavity opto-magnonics for microwave-to-optics conversion, Optica **7**, 1291 (2020).
[13] K. V. Adwaith, A. Karigowda, C. Manwatkar, F. Bretenaker, and A. Narayanan, Coherent microwave-to-optical conversion by three-wave mixing in a room temperature atomic system, Opt. Lett. **44**, 33 (2019).
[14] T. Vogt, C. Gross, J. Han, S. B. Pal, M. Lam, M. Kiffner, and W. Li, Efficient microwave-to-optical conversion using Rydberg atoms, Phys. Rev. A **99**, 023832 (2019).
[15] A. Kumar, A. Suleymanzade, M. Stone, L. Taneja, A. Anferov, D. I. Schuster, and J. Simon, Quantum-enabled millimetre wave to optical transduction using neutral atoms, Nature (London) **615**, 614 (2023).
[16] M. Tsang, Cavity quantum electro-optics, Phys. Rev. A **81**, 063837 (2010).
[17] M. Tsang, Cavity quantum electro-optics. II. Input-output relations between traveling optical and microwave fields, Phys. Rev. A **84**, 043845 (2011).
[18] A. Rueda *et al.*, Efficient microwave to optical photon conversion: An electro-optical realization, Optica **3**, 597 (2016).
[19] W. Hease, A. Rueda, R. Sahu, M. Wulf, G. Arnold, H. G. L. Schwefel, and J. M. Fink, Bidirectional electro-optic wavelength conversion in the quantum ground state, PRX Quantum **1**, 020315 (2020).
[20] R. Sahu, W. Hease, A. Rueda, G. Arnold, L. Qiu, and J. M. Fink, Quantum-enabled operation of a microwave-optical interface, Nat. Commun. **13**, 1276 (2022).
[21] C. Wang, I. Gonin, A. Grassellino, S. Kazakov, A. Romanenko, V. P. Yakovlev, and S. Zorzetti, High-efficiency microwave-optical quantum transduction based on a cavity electro-optic superconducting system with long coherence time, npj Quantum Inf. **8**, 1 (2022).
[22] L. Fan, C.-L. Zou, R. Cheng, X. Guo, X. Han, Z. Gong, S. Wang, and H. X. Tang, Superconducting cavity electro-optics: A platform for coherent photon conversion between superconducting and photonic circuits, Sci. Adv. **4**, eaar4994 (2018).
[23] J. Holzgrafe, N. Sinclair, D. Zhu, A. Shams-Ansari, M. Colangelo, Y. Hu, M. Zhang, K. K. Berggren, and M. Lončar, Cavity electro-optics in thin-film lithium niobate for efficient microwave-to-optical transduction, Optica **7**, 1714 (2020).
[24] T. P. McKenna, J. D. Witmer, R. N. Patel, W. Jiang, R. V. Laer, P. Arrangoiz-Arriola, E. A. Wollack, J. F. Herrmann, and A. H. Safavi-Naeini, Cryogenic microwave-to-optical conversion using a triply resonant lithium-niobate-on-sapphire transducer, Optica **7**, 1737 (2020).
[25] Y. Xu, A. A. Sayem, L. Fan, C.-L. Zou, S. Wang, R. Cheng, W. Fu, L. Yang, M. Xu, and H. X. Tang, Bidirectional interconversion of microwave and light with thin-film lithium niobate, Nat. Commun. **12**, 4453 (2021).
[26] M. Pechal and A. H. Safavi-Naeini, Millimeter-wave interconnects for microwave-frequency quantum machines, Phys. Rev. A **96**, 042305 (2017).
[27] A. Anferov, A. Suleymanzade, A. Oriani, J. Simon, and D. I. Schuster, Millimeter-wave four-wave mixing via kinetic inductance for quantum devices, Phys. Rev. Appl. **13**, 024056 (2020).
[28] M. Xu, X. Han, C.-L. Zou, W. Fu, Y. Xu, C. Zhong, L. Jiang, and H. X. Tang, Radiative cooling of a superconducting resonator, Phys. Rev. Lett. **124**, 033602 (2020).
[29] S. Mobassem, N. J. Lambert, A. Rueda, J. M. Fink, G. Leuchs, and H. G. L. Schwefel, Thermal noise in electro-optic devices at cryogenic temperatures, Quantum Sci. Technol. **6**, 045005 (2021).
[30] J. P. Pekola and B. Karimi, Colloquium: Quantum heat transport in condensed matter systems, Rev. Mod. Phys. **93**, 041001 (2021).
[31] W. Koechner, Thermo-optic effects, in *Solid-State Laser Engineering*, edited by W. Koechner (Springer, New York, 2006), pp. 423–487.
[32] J. R. Tucker and M. J. Feldman, Quantum detection at millimeter wavelengths, Rev. Mod. Phys. **57**, 1055 (1985).
[33] R. J. Schoelkopf, S. H. Moseley, C. M. Stahle, P. Wahlgren, and P. Delsing, A concept for a submillimeter-wave single-photon counter, IEEE Trans. Appl. Supercond. **9**, 2935 (1999).
[34] J. Zmuidzinas and P. L. Richards, Superconducting detectors and mixers for millimeter and submillimeter astrophysics, Proc. IEEE **92**, 1597 (2004).
[35] J. Li, M. Takeda, Z. Wang, S.-C. Shi, and J. Yang, Low-Noise 0.5 THz all-NbN superconductor-insulator-superconductor mixer for submillimeter wave astronomy, Appl. Phys. Lett. **92**, 222504 (2008).
[36] J. W. Kooi *et al.*, Quantum limited SIS receiver technology for the detection of water isotopologue emission from comets, IEEE Trans. Terahertz Sci. Technol. **10**, 569 (2020).
[37] B. Ho Eom, P. K. Day, H. G. LeDuc, and J. Zmuidzinas, A Wideband, low-noise superconducting amplifier with high dynamic range, Nat. Phys. **8**, 623 (2012).
[38] S. Goldstein, N. Kirsh, E. Svetitsky, Y. Zamir, O. Hachmo, C. E. M. de Oliveira, and N. Katz, Four wave-mixing in a microstrip kinetic inductance travelling wave parametric amplifier, Appl. Phys. Lett. **116**, 152602 (2020).
[39] M. Malnou, M. R. Vissers, J. D. Wheeler, J. Aumentado, J. Hubmayr, J. N. Ullom, and J. Gao, Three-wave mixing kinetic inductance traveling-wave amplifier with near-quantum-limited noise performance, PRX Quantum **2**, 010302 (2021).
[40] B.-K. Tan, N. Klimovich, R. Stephenson, F. Faramarzi, and P. Day, Operation of kinetic-inductance travelling wave parametric amplifiers at millimetre wavelengths, Supercond. Sci. Technol. **37**, 035006 (2024).
[41] C. Javerzac-Galy, K. Plekhanov, N. R. Bernier, L. D. Toth, A. K. Feofanov, and T. J. Kippenberg, On-chip microwave-to-optical quantum coherent converter based on a superconducting resonator coupled to an electro-optic microresonator, Phys. Rev. A **94**, 053815 (2016).
[42] M. Soltani, M. Zhang, C. Ryan, G. J. Ribeill, C. Wang, and M. Loncar, Efficient quantum microwave-to-optical conversion using electro-optic nanophotonic coupled resonators, Phys. Rev. A **96**, 043808 (2017).
[43] A. Guarino, G. Poberaj, D. Rezzonico, R. Degl'Innocenti, and P. Günter, Electro–optically tunable microring resonators in lithium niobate, Nat. Photonics **1**, 407 (2007).

[44] C. Wang, M. Zhang, B. Stern, M. Lipson, and M. Lončar, Nanophotonic lithium niobate electro-optic modulators, Opt. Express **26**, 1547 (2018).
[45] A. Boes, B. Corcoran, L. Chang, J. Bowers, and A. Mitchell, Status and potential of lithium niobate on insulator (LNOI) for photonic integrated circuits, Laser Photonics Rev. **12**, 1700256 (2018).
[46] M. Bahadori, M. Nikdast, S. Rumley, L. Y. Dai, N. Janosik, T. Van Vaerenbergh, A. Gazman, Q. Cheng, R. Polster, and K. Bergman, Design space exploration of microring resonators in silicon photonic interconnects: Impact of the ring curvature, J. Light. Technol. **36**, 2767 (2018).
[47] R. D. Delaney, M. D. Urmey, S. Mittal, B. M. Brubaker, J. M. Kindem, P. S. Burns, C. A. Regal, and K. W. Lehnert, Superconducting-qubit readout via low-backaction electro-optic transduction, Nature (London) **606**, 489 (2022).
[48] L. Qiu, R. Sahu, W. Hease, G. Arnold, and J. M. Fink, Coherent optical control of a superconducting microwave cavity via electro-optical dynamical back-action, Nat. Commun. **14**, 3784 (2023).
[49] T. C. Zhang, K. W. Goh, C. W. Chou, P. Lodahl, and H. J. Kimble, Quantum teleportation of light beams, Phys. Rev. A **67**, 033802 (2003).
[50] M. Zhang, C.-L. Zou, and L. Jiang, Quantum transduction with adaptive control, Phys. Rev. Lett. **120**, 020502 (2018).
[51] J. Wu, C. Cui, L. Fan, and Q. Zhuang, Deterministic microwave-optical transduction based on quantum teleportation, Phys. Rev. Appl. **16**, 064044 (2021).
[52] A. S. Holevo and R. F. Werner, Evaluating capacities of bosonic Gaussian channels, Phys. Rev. A **63**, 032312 (2001).
[53] M. Rosati, A. Mari, and V. Giovannetti, Narrow bounds for the quantum capacity of thermal attenuators, Nat. Commun. **9**, 4339 (2018).
[54] M. Fanizza, F. Kianvash, and V. Giovannetti, Estimating quantum and private capacities of Gaussian channels via degradable extensions, Phys. Rev. Lett. **127**, 210501 (2021).
[55] S. Pirandola, R. Laurenza, C. Ottaviani, and L. Banchi, Fundamental limits of repeaterless quantum communications, Nat. Commun. **8**, 15043 (2017).
[56] C.-H. Wang, F. Li, and L. Jiang, Quantum capacities of transducers, Nat. Commun. **13**, 6698 (2022).
[57] J. Keller, G. Scalari, F. Appugliese, E. Mavrona, S. Rajabali, M. J. Süess, M. Beck, and J. Faist, High $T_c$ superconducting THz metamaterial for ultrastrong coupling in a magnetic field, ACS Photonics **5**, 3977 (2018).
[58] A. K. Hamze, M. Reynaud, J. Geler-Kremer, and A. A. Demkov, Design rules for strong electro-optic materials, npj Comput. Mater. **6**, 1 (2020).
[59] W. Heni *et al.*, Silicon–organic and plasmonic–organic hybrid photonics, ACS Photonics **4**, 1576 (2017).
[60] P. B. Deotare, M. W. McCutcheon, I. W. Frank, M. Khan, and M. Lončar, High quality factor photonic crystal nanobeam cavities, Appl. Phys. Lett. **94**, 121106 (2009).
[61] S. Hähnle, K. Kouwenhoven, B. Buijtendorp, A. Endo, K. Karatsu, D. J. Thoen, V. Murugesan, and J. J. A. Baselmans, Superconducting microstrip losses at microwave and submillimeter wavelengths, Phys. Rev. Appl. **16**, 014019 (2021).
[62] I.-C. Benea-Chelmus, Y. Salamin, F. F. Settembrini, Y. Fedoryshyn, W. Heni, D. L. Elder, L. R. Dalton, J. Leuthold, and J. Faist, Electro-optic interface for ultrasensitive intracavity electric field measurements at microwave and terahertz frequencies, Optica **7**, 498 (2020).
[63] F. Faramarzi, P. Day, J. Glasby, S. Sypkens, M. Colangelo, R. Chamberlin, M. Mirhosseini, K. Schmidt, K. K. Berggren, and P. Mauskopf, Initial design of a W-band superconducting kinetic inductance qubit, IEEE Trans. Appl. Supercond. **31**, 1 (2021).
[64] A. Anferov, S. P. Harvey, F. Wan, J. Simon, and D. I. Schuster, Superconducting qubits above 20 GHz operating over 200 mK, arXiv:2402.03031.
[65] A. Pascual Laguna, K. Karatsu, D. J. Thoen, V. Murugesan, B. T. Buijtendorp, A. Endo, and J. J. A. Baselmans, Terahertz band-pass filters for wideband superconducting on-chip filter-bank spectrometers, IEEE Trans. Terahertz Sci. Technol. **11**, 635 (2021).
[66] M. Burla *et al.*, Plasmonics for microwave photonics in the THz range, Front. Photonics **4**, 1067916 (2023).
[67] J. Liu *et al.* (BREAD Collaboration), Broadband solenoidal haloscope for terahertz axion detection, Phys. Rev. Lett. **128**, 131801 (2022).
[68] E. T. Khabiboulline, J. Borregaard, K. De Greve, and M. D. Lukin, Optical interferometry with quantum networks, Phys. Rev. Lett. **123**, 070504 (2019).
[69] C. Joshi, W. Chen, H. G. LeDuc, P. K. Day, and M. Mirhosseini, Strong kinetic-inductance kerr nonlinearity with titanium nitride nanowires, Phys. Rev. Appl. **18**, 064088 (2022).
[70] M. J. Lancaster, *Passive Microwave Device Applications of High-Temperature Superconductors* (Cambridge University Press, Cambridge, 1997).
[71] A. Tsiatmas, V. A. Fedotov, F. J. G. de Abajo, and N. I. Zheludev, Low-loss terahertz superconducting plasmonics, New J. Phys. **14**, 115006 (2012).
[72] U. S. Pracht *et al.*, Electrodynamics of the superconducting state in ultra-thin films at THz frequencies, IEEE Trans. Terahertz Sci. Technol. **3**, 269 (2013).
[73] W. Zimmermann, E. H. Brandt, M. Bauer, E. Seider, and L. Genzel, Optical conductivity of BCS superconductors with arbitrary purity, Phys. C (Amsterdam) **183**, 99 (1991).
[74] V. Musilová, T. Králík, T. Fořt, and M. Macek, Strong suppression of near-field radiative heat transfer by superconductivity in NbN, Phys. Rev. B **99**, 024511 (2019).
[75] A. Semenov *et al.*, Optical and transport properties of ultrathin NbN films and nanostructures, Phys. Rev. B **80**, 054510 (2009).
[76] J. Zmuidzinas, Superconducting microresonators: Physics and applications, Annu. Rev. Condens. Matter Phys. **3**, 169 (2012).
[77] E. Scarano, E. K. Arvidsson, A. K. Roos, E. Holmgren, and D. B. Haviland, Temperature dependence of microwave losses in lumped-element resonators made from superconducting nanowires with high kinetic inductance, arXiv:2401.02943.
[78] B. E. Little, S. T. Chu, H. A. Haus, J. Foresi, and J.-P. Laine, Microring resonator channel dropping filters, J. Light. Technol. **15**, 998 (1997).
[79] K. Guo, X. Shi, X. Wang, J. Yang, Y. Ding, H. Ou, and Y. Zhao, Generation rate scaling: The quality factor optimization of microring resonators for photon-pair sources, Photonics Res. **6**, 587 (2018).
[80] M. A. Fakhri, Y. Al-Douri, A. Bouhemadou, and M. Ameri, Structural and optical properties of nanophotonic $LiNbO_3$ under stirrer time effect, J. Opt. Commun. **39**, 297 (2018).
[81] X. Wu, C. Zhou, W. R. Huang, F. Ahr, and F. X. Kärtner, Temperature dependent refractive index and absorption coefficient

of congruent lithium niobate crystals in the terahertz range, Opt. Express **23**, 29729 (2015).

[82] S. Zorzetti, C. Wang, I. Gonin, S. Kazakov, T. Khabiboulline, A. Romanenko, V. P. Yakovlev, and A. Grassellino, Millikelvin measurements of permittivity and loss tangent of lithium niobate, Phys. Rev. B **107**, L220302 (2023).

[83] A. M. Glass and J. Strait, The photorefractive effect in semiconductors, in *Photorefractive Materials and Their Applications I: Fundamental Phenomena*, edited by P. Günter and J.-P. Huignard (Springer, Berlin, 1988), pp. 237–262.

[84] R. C. Zeller and R. O. Pohl, Thermal conductivity and specific heat of noncrystalline solids, Phys. Rev. B **4**, 2029 (1971).

[85] B. Bonin, Materials for superconducting cavities, in Conference: CERN Accelerator School, Superconductivity in Particle Accelerators, CEA-DAPNIA-SEA-96-02, CONF-9505411, 1996.

[86] A. D. Semenov, G. N. Gol'tsman, and A. A. Korneev, Quantum detection by current carrying superconducting film, Phys. C (Amsterdam) **351**, 349 (2001).

[87] E. Pérez-Enciso and S. Vieira, Thermal properties of intrinsically disordered $LiNbO_3$ crystals at low temperatures, Phys. Rev. B **57**, 13359 (1998).

[88] B. T. Matthias, Transition temperatures of superconductors, Phys. Rev. **92**, 874 (1953).